J Mater Sci (2007) 42:7202–7213
DOI 10.1007/s10853-006-1422-8

Polymeric foam deformation under dynamic loading by the use of the microtomographic technique

Philippe Viot · Dominique Bernard · Erwan Plougonven

Received: 13 July 2006 / Accepted: 11 December 2006 / Published online: 10 May 2007

Abstract The mechanical behaviour of polymeric foams depends on several parameters such as temperature, material density and strain rate. This last point implies that compression tests on conventional testing machines are not sufficient. Study of the behaviour in practical situations requires special apparatus like fly wheels, drop towers or Hopkinson bars, allowing high compression speeds. The polypropylene foams studied are multi-scale materials; agglomerated beads (2–3 mm in diameter), visible to the naked eye, are composed of microscopic closed cells (a few tens of microns). The response of the material to a shock consists of three regions: an elastic phase, a plastic phase and densification. The plastic phase is of prime interest since a great part of the shock energy is dissipated there. Microtomography was used in order to better understand damage mechanisms during the stress plateau of the plastic phase. The final objective of this work is to determine the strain field of porous materials at several levels of shock. As tomography is not fast enough to directly follow the impact deformation, interrupted impact tests were carried out by controlling the levels of sample deformation. Between each impact step, a microtomographic analysis offers insight on the progressive deformation of the sample. The results of these impact tests completed by a microtomographic visualisation in 2D are presented and commented in this paper.

P. Viot (✉)
LAMEFIP, ENSAM de Bordeaux, Esplanade des arts et métiers, 33405 Talence Cedex, France
e-mail: philippe.viot@lamef.bordeaux.ensam.fr

D. Bernard · E. Plougonven
ICMCB, CNRS, Univ. Bordeaux1, 87 av. du Dr A. Schweitzer, 33608 Pessac, France

Introduction

Cellular materials are used in many passive security applications: for example transport of fragile materials (electronics, aeronautic structures), food packaging, and personal protective gear (life jackets, helmets, knee pads).

In the development process, numerical tools are used more and more to design the product and optimise its performances in terms of energy absorption during a shock, even if knowledge of the cellular material is poor. In order to improve the results of these models (and answer engineering and design requirements), it is necessary to better understand, model and identify the behaviour of cellular materials used.

Many studies have been carried out at the macroscopic scale to characterise the behaviour of this type of material under dynamic stresses [1–5]. Empirical laws were proposed to rapidly answer engineering requirements. The observed phenomena are more or less accurately integrated in these laws that often describe the relation between stress and strain according to different parameters such as density, temperature, etc. The behaviour of cellular materials generally includes three steps in static or dynamic compression: an elastic response followed by an important deformation of the material with quasi-constant stress, and a densification. It is the stress plateau of the plastic phase that is of interest for passive security applications since the material can absorb a significant fraction of the impact kinetic energy.

The macroscopic laws used in finite element codes can coarsely describe the macroscopic behaviour of cellular materials (in the elastic and stress plateau phases) but do not take into account the localisations of the observed strains—and thus their heterogeneity. These laws, used in industry and numerically adjusted on the global stress curves, can be used to represent the behaviour of a large

variety of cellular materials such as polymeric or aluminium foams. It is well known that for the former, the predominant phenomenon in its damage is wall buckling of the constitutive cells whereas wall fractures can be observed in the latter. It is therefore essential to propose macroscopic behaviour models which take into account the physical phenomena observed at all scales (macro-, meso- and micro-scale) of the cellular material structure.

The material studied is a polypropylene foam. The plates of cellular material, provided by PACTUCO, are obtained by moulding; the expanded plastic foam beads are injected into a plate mould (700 mm × 400 mm × 24 mm), where individual beads are fused together under steam heat and pressure. The average density of each plate intrinsically depends on the quantity of expanded beads injected into the mould. For this study, the density of the plate is 80 kg/m^3. The moulding process, particularly the injector and vent positions, induces density heterogeneities. Horizontally, measurements on a large number of samples cut out from this plate show values as large as 92 kg/m^3. Vertically, i.e., through the thickness of the plate, the density increases significantly near the surfaces (12%), whereas in the central region it is relatively uniform. Consequently, the samples selected (10 mm in diameter and height) were taken from the centre of the plate (Fig. 1a). The sample studied in this paper has a density of 80 kg/m^3.

The structure of the polymeric foam studied here is multi-scale (Fig. 1b and c). At the mesoscopic scale, the material consists of porous beads of polypropylene agglomerated during manufacturing. The average diameter of these beads is 2 mm. SEM pictures carried out in different sections of the cellular material (Fig. 1b) indicate that the size of the grains is relatively homogeneous and that their geometries do not show any preferential orientation. This is confirmed by the first microtomographic reconstruction of a slice of the undeformed sample (Fig. 5c); the polyhedral shape of the beads is equi-axed. The beads are composed of much smaller closed cells (microscopic scale) of about 60 μm in diameter, with a wall thickness close to 1 μm. The response of this polymeric foam under dynamic loading depends on the constitutive material (polypropylene) and on its multi-scale structure.

This study is part of a work whose aim is to propose a behaviour model taking into account the physics of the phenomena observed during dynamic loading. The evolution of cellular materials under stress is foreseen by a multi-scale description. It is obviously necessary to identify the global response of materials at the macroscopic scale for various strain rates, but also to investigate the response of the foam structure at the mesoscopic (that of the bead) and microscopic scales (that of the basic cell). Observation of the deformation of the meso- and microscopic walls (bead and cell) will be one of the elements that will help to establish phenomenological laws at these scales. Homogenisation methods will then be used to build a model describing the foam response at the macroscopic scale. The first step of this methodology, described in this article, is

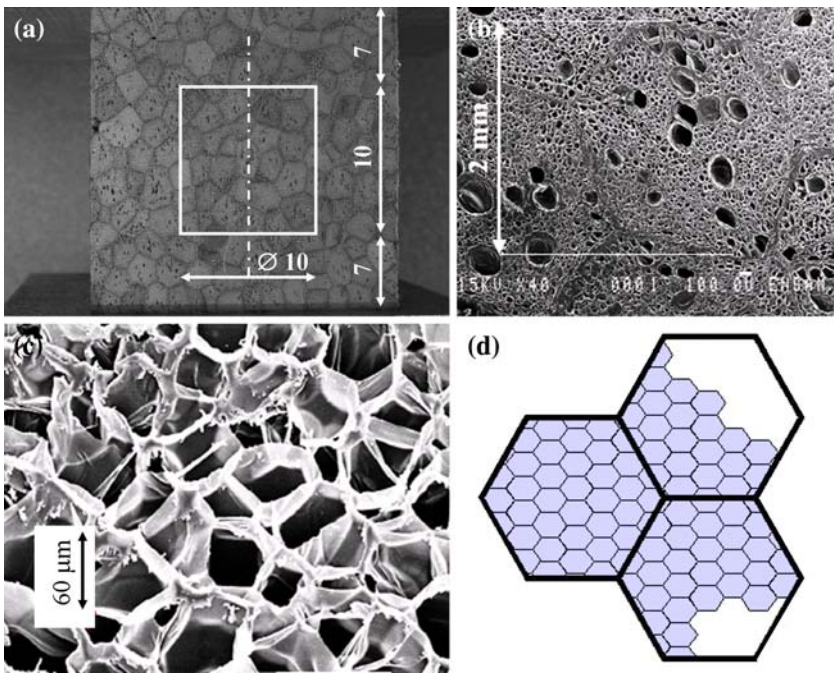

Fig. 1 (**a**) Position of the sample in the foam plate; (**b**) Micrograph of polypropylene foam showing the bead structure; (**c**) Micrograph of polypropylene foam showing the cell structure; (**d**) Multi-scale model of the foam structure

the observation, the comprehension and the characterisation of the physical phenomena. This step is essential to reach the final objective of foam structure modelling. It is then planned to represent in finite element code the polymeric foam by a polyhedral structure taking into account the two meso- and microscopic scales of the material (Fig. 1d). A macroscopic model would then be proposed.

Methodology and experimental apparatus

The physical phenomena observed on polymeric foams during dynamic compression has already been studied under specific conditions [6]. After impact, the buckling of both cell and bead walls have been observed by SEM. A strong heterogeneity of the residual deformation can be seen. However, the main difficulty of these observations lies in the sample cutting. Until recently it was impossible to measure the buckling phenomena inside the sample without a preliminary slicing, causing damage often as important as the damage to be estimated.

Complementary measurements were taken during impact with the use of optical acquisition apparatus and image processing techniques (high-speed camera, optical fibre spotlights and Digital Image Correlation software). A strong heterogeneity of the strain field was shown, and strain localisations appear in layers perpendicular to the loading direction. The material damage progresses close to these zones in the stress plateau [5, 7]. However these observations are only possible on the sample free face, implying that this method cannot estimate the strain field inside the foam structure. In the light of these first results, microtomography was considered for observing the deformation inside the foam structure. This technique allows characterising in three dimensions the structure of a heterogeneous material with a high degree of accuracy. However, an acquisition can take 60 min which is incompatible with the usual dynamic tests that do not exceed a few milliseconds. Identifying foam deformation and damage propagation in 3D needs an original dynamic test methodology complying with microtomography requirements [8]. This article presents the procedure and the first results.

The adopted experimental approach consists in carrying out several interrupted impact tests on a given sample using a drop tower, and acquiring a microtomography in between each impact. An image of the sample (diameter and height of 10 mm) is taken before the first impact. During compression, the deformation amplitude is limited to fixed values: 1 mm for the first impact and 2 mm for the following ones. The sample is maintained compressed and replaced on the microtomography setup for another acquisition (point A, Fig. 2). The blocking device principle

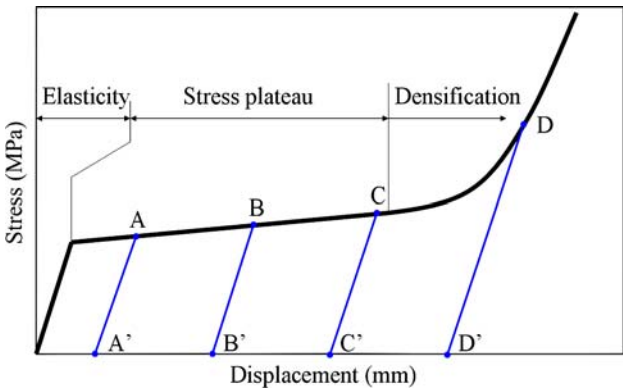

Fig. 2 Typical evolution of compression stress versus strain for a cellular material

has been validated since no local deformation was observed during the time of acquisition. These operations (impact and X-ray scan) are repeated until densification of the foam (points B, C and D, where the sample is respectively 7, 5 and 3 mm high). The cellular material deformation can then be evaluated from the 3D reconstructions at each stage of the dynamic test.

Impact apparatus

The experimental procedure requires that impact tests be carried out near the microtomography setup. A portative drop tower for interrupted impacts was specially designed for this purpose. It includes two subsets: a loading module and a measurement device (Fig. 3). The loading module consists in a 0.37 kg cylindrical projectile guided in a

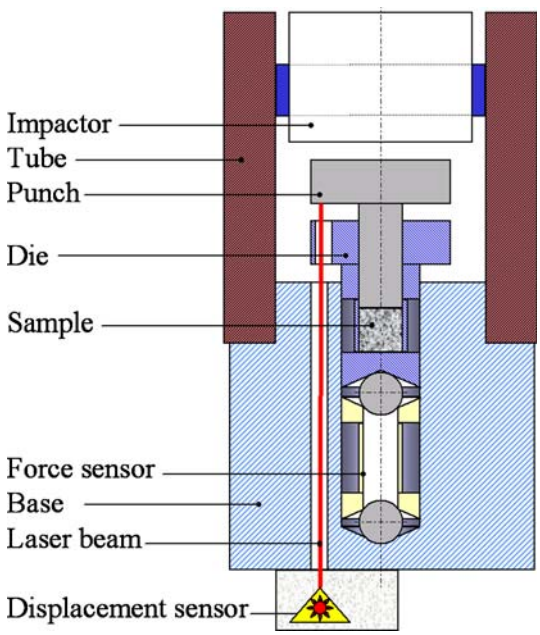

Fig. 3 Drop tower apparatus

ground metallic tube of 1.6 m high. The tube is placed above the measurement module, which consists of an aluminium base, a die-punch set and sensors for displacement and force. The sample is placed inside the die and compressed by the punch.

During the impact test, the projectile is dropped in the tube with no initial speed and falls freely. It strikes the punch, which compresses the sample into the die. At the beginning of the impact, the measured speed of the punch is 5 m/s. The punch speed is constant during the compression since the projectile energy is substantially higher than the energy dissipated in the foam deformation.

Several punches of different lengths (16, 18, 20 and 22 mm) are used to carry out successive compressions. The die-punch set was designed in order to apply uniaxial compression on the foam sample and also to be easily removed out of the drop tower and placed on the micro-tomographic setup. After an impact, the punch shoulder stays against the die to keep the sample compressed during the tomographic measurement.

This device is instrumented to measure the compression force and the macroscopic sample deformation during the test. The punch displacement is obtained from a laser sensor. Assuming an infinitely rigid device, the sample strain and strain rate can be calculated. To complete (and verify) this measurement, impacts are recorded using a high-speed camera Phantom V4 (frequency of 5,000 frames per second, resolution of 128 × 256 pixels). The punch displacement can be obtained by analysing a marker position on each image. To evaluate the impact force, a sensor (placed just below the die) made of an aluminium tube (7 mm in diameter and 0.2 mm thick) and 4 gauges connected in a Wheatstone bridge. The relation between force and measured signal is obtained from calibration.

Microtomography principle

Consider a homogeneous material characterised by μ, its linear attenuation coefficient, and illuminated by a monochromatic beam of energy E. The ratio between N_0, the number of incident photons, and N, the number of photons transmitted through the material thickness L is given by Beer–Lambert's law [9]:

$$N = N_0 e^{[-\mu L]} \tag{1}$$

For a heterogeneous material, μL must be replaced by the integral of μ along the photon path. The number of transmitted photon N is then:

$$N = N_0 e^{\left(-\int_{\text{path}L} \mu(l)\mathrm{d}l\right)} \tag{2}$$

By measuring N_0 and N the above integral of μ can be calculated:

$$\ln\frac{N_0}{N} = \int_{\text{path}L} \mu(l)\mathrm{d}l \tag{3}$$

Let us now consider an object characterised by its 3D mapping $\mu(x, y, z)$. We place it, as seen in Fig. 4, on a rotation table (z is the rotation axis) in the X-ray beam (direction v) and before the 2D detector (plane (u, z), with u perpendicular to v).

Each section perpendicular to z can be considered individually because the synchrotron beam is parallel. For an angular position θ of the object, N can be measured at each point u on the detector and relation (4) can be used to calculate the projection P:

$$\begin{aligned} P(\theta) &= \{P(u,\theta)\ ;\ u \in [-r;r]\} \\ &= \left\{ \ln\left(\frac{N_0(u)}{N(u)}\right) = \int_{\text{ray}u} \mu(v)\mathrm{d}v; u \in [-r;r] \right\} \end{aligned} \tag{4}$$

Where $-r$ and r represent the limits of u on the detector, and ray u the line parallel to v hitting the detector at u. The set of projections $P(\theta)$ for θ varying between 0° and 180° is Radon's transform of $\mu(x, y)$. In 1917, Radon proved mathematically that it is possible to invert this transform and thus it is possible to reconstruct the 3D map of μ from a set of projections [10, 11].

Given a pure material it is possible, from the calculated 3D map of the linear attenuation coefficient μ [cm^{-1}], to obtain a 3D image of the material since the mass attenuation coefficient μ/ρ is correlated to the photon energy E and the atomic number Z. For energies lower than 200 keV, the following relation can be used:

$$\frac{\mu}{\rho} = K\frac{Z^4}{E^3} \tag{5}$$

where ρ is the material density [g/cm^3] and K a constant. Equation (5) implies that at a given energy E (an adjustable

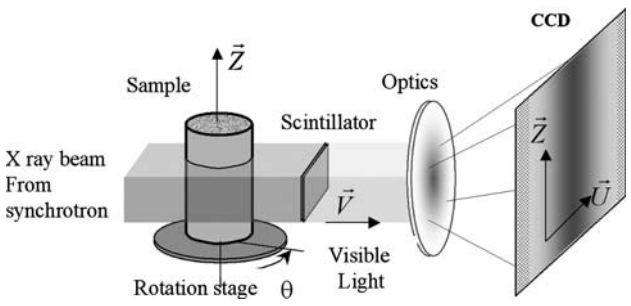

Fig. 4 Scheme of the microtomographic apparatus

parameter in synchrotron tomography), the linear attenuation coefficient μ is proportional to ρ and Z^4.

The mass attenuation coefficient μ/ρ of a heterogeneous material containing i elements (mass concentration w_i with specific mass attenuation coefficient $(\mu/\rho)_i$) is obtained with the following relation:

$$\frac{\mu}{\rho} = \sum w_i \left(\frac{\mu}{\rho}\right)_i \tag{6}$$

X-ray computed tomography then consists in detecting the residual energy of a beam that crosses through a sample (a radiograph giving N) for a large number of different angles (between 900 and 1,500 radiographs on 180°. Some reference images are added to control the noise and the homogeneity of the incident beam, which gives N_0. The 3D representation of the X-ray absorption by the sample is then numerically reconstructed from all these 2D images. The most commonly used algorithm for reconstruction is the filtered back-projection method [9].

At a given energy, absorption of X-rays is function of several physical parameters, mainly the local density and the atomic number of the crossed material. In a porous material, if all the components of the solid phase have about the same X-ray absorption, the 3D image of the absorption can be transformed into an image of the porosity. The use of microtomography in material science thus requires that the studied material present differences of internal absorption, which can be measured within the studied volume elements (voxels).

The data presented in this paper have been obtained on the BM05 beam line at the European Synchrotron Radiation Facility (ESRF) in Grenoble (France). The tomographic apparatus available on BM05 allow the acquisition of 1,024 × 1,024 or 2,028 × 2,048 pixels radiographs with pixel sizes ranging from 40 µm to 2 µm. The selected optical setup placed after the scintillator that converts, as efficiently as possible, X-rays to visible light fixes this pixel size. Those parameters also determine the size of the sample. Indeed, in classical tomography, samples must have a maximal lateral size such that the projections match the field of view of the digital camera. The maximum size is then equal to the pixel size multiplied by the number of pixels on a row of the detector. For small foam samples with a diameter less than 0.8 mm, as the one shown in Fig. 5a, the tomographic device allows us to visualise in 3D the cell morphology of the polypropylene foam (Fig. 5b). For our study, because impacts have to be done on samples representative of the foam structure, the selected sample diameter was 10 mm for 2,048 pixels on the acquired radiographs. With this size it is not possible to visualise the cells with a good accuracy but it is sufficient for larger bead walls (Fig. 5c).

The sample diameter being fixed to 10 mm, the energy E has been adjusted according to material absorption in order to obtain images with the best contrast. For an optimal energy of 16 keV, the height of the X-ray beam was about 5 mm. For higher samples, two scans at different heights were performed. Sample displacement accuracy is much better than the pixel size and merging the two scans to obtain a 3D image of the complete sample was easily done in post processing.

The successive operations of impact carried out on the drop tower require the sample to be removed from the microtomographic table. A pin placed on the die axis and a visual marker plotted on the die facilitate the sample placement roughly in the same position for all the scans. Nevertheless, numerical adjustment of the angular positions of all the microtomographies was necessary in order to evaluate the displacement and the

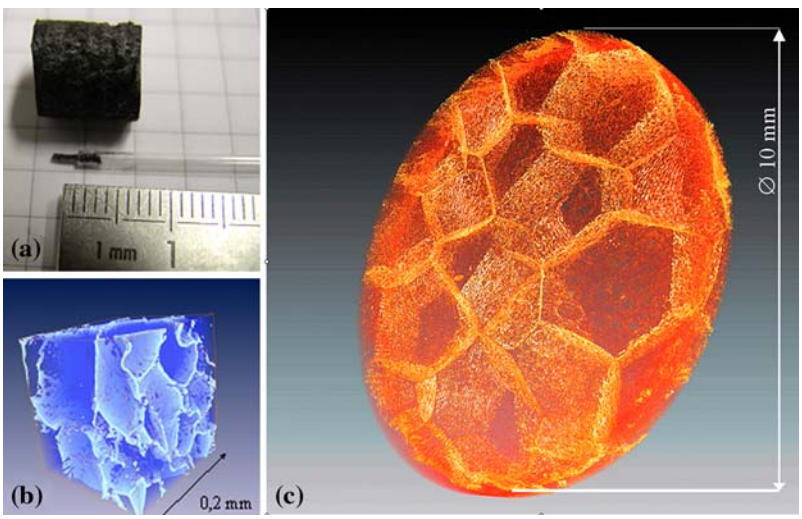

Fig. 5 (**a**) Picture of two samples (sample used for impact test and small sample scanned at high resolution 0.28 µm); (**b**) A microtomographic view of the small sample; (**c**) A microtomographic view of the large sample

deformation of each bead. To do so, the following method was applied: for a cylindrical section S_{ref} calculated on the intact sample (used as a reference) the best corresponding deformed section S_{def} of the sample after the first impact (noted sample 9) was visually determined. The two sections are added together to obtain a control image S_c (Fig. 6a) that reveals the angular mismatch between the section S_{def} and the reference section S_{ref}. The difference of angular position of the two sections can clearly be seen: the walls of the beads located on the periphery of the sample do not coincide.

Rotating section S_{def} by small increments before the addition with the reference section S_{ref} results in a series of control images. Plotting the average grey level of control images as a function of the rotation angle (Fig. 7a) gives a curve whose maximum indicates the optimal rotation angle. Figure 6b shows the control image S_c corresponding to this optimal angle. Note that the walls of the beads between the two images are very close, and that almost no deformation appears, since the sample is still in its elastic phase.

Finding the optimal rotation angle becomes more difficult when compression proceeds (heights 7, 5 and 3 mm). For these images, the visual selection of section S_{def} is very arduous. In consequence, the operations carried out between deformed and reference sections were repeated for several deformed sections in the vicinity of the estimated section S_{def}. The measurement of the grey level average for each stage provides a set of curves (Fig. 7b) having each one an extremum. The maximum of these maxima is a criterion for choosing the deformed section that best corresponds to the reference section, and thus the optimal angular position. The angular variations are relatively low (less than 3 degrees) but it was necessary to have a unique coordinate system (O,x,y,z) for all the images so as to evaluate the 3D deformation of the foam structure as accurately as possible.

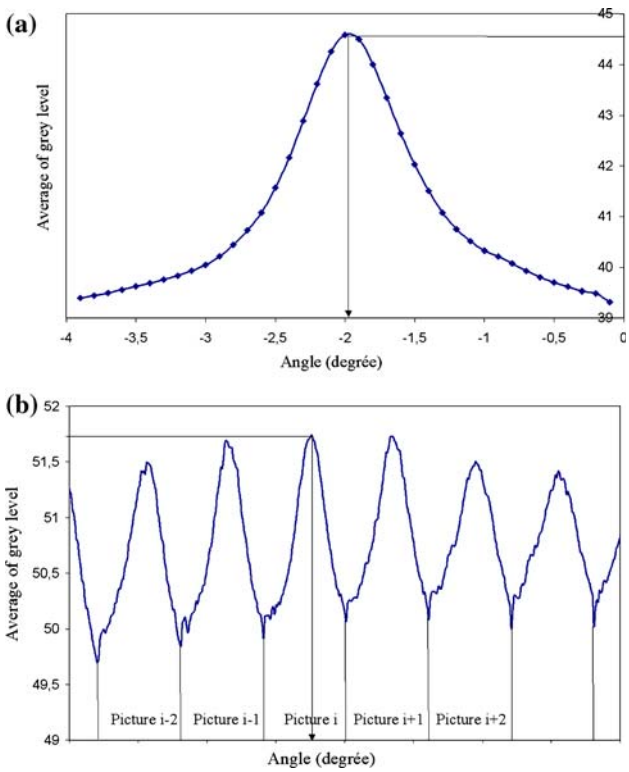

Fig. 7 (**a**) Evolution of the average grey level of the control picture (addition of the reference section and equivalent section after the first impact) as a function of calibration rotation angle; (**b**) Evolution of the average grey level of the control picture (addition of the reference section and different sections i after the second impact) as a function of calibration rotation angle

Results

Macroscopic behaviour

Figure 8 shows the displacement-force curve obtained during the first tests of the impact apparatus. From these results and given the sample dimensions, it is possible to obtain the evolution of the average stress according to the

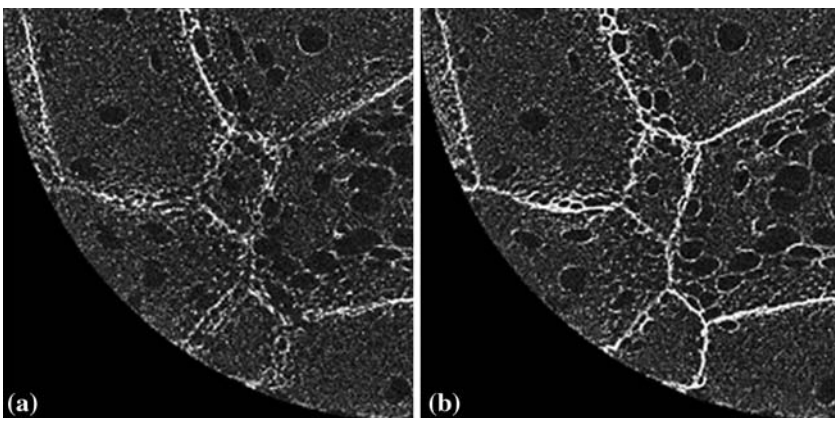

Fig. 6 (**a**) Result of the addition of two sections (reference position before impact and position after the first impact) and before numerical rotation; (**b**) Result of the addition of two sections (reference position before impact and position after the first impact) after calibration of the rotation angle

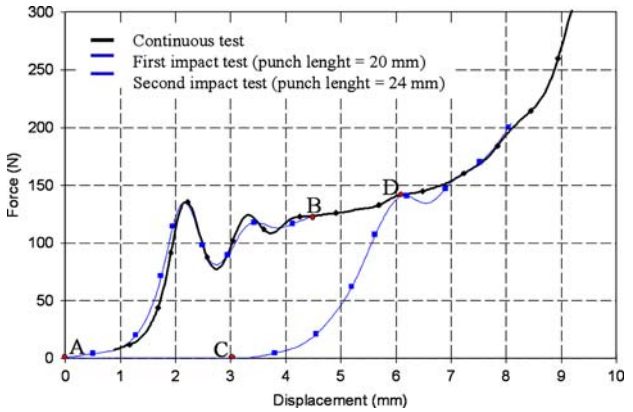

Fig. 8 Force-displacement curves of impacts on polypropylene sample (continuous and interrupted tests)

global strain. One of the results of this article being the strong heterogeneity of the deformation in the sample, it was not relevant to define a local strain from macroscopic measurements. Similarly, in a structure as complex as that of a cellular material, the local stress depends on the force field applied on the cell and bead walls and cannot be estimated directly by the signal of a force sensor. We therefore preferred to represent the foam behaviour in terms of force vs. displacement.

A first uninterrupted test (black line) was carried out in order to determine the three regimes of the foam behaviour: The linear-elastic part followed by a collapse plateau, and finally the densification.

The second test (blue curve) consisted of two successive impacts: The first impact (curve AB) covers the elastic stage and the beginning of the stress plateau. The loading was interrupted at point B, and the sample, returning to point C, still presents some elasticity with a substantial rebound displacement. After this first impact the sample deformation (distance AC) was of 2.9 mm. For the second impact, starting at point C, the elastic behaviour (zone CD) appears to be less rigid. After this new elastic stage, the foam returns to a stress plateau at about the same force as the one of the first sample (continuous test), and continues on a similar curve.

Force measurements obtained from this drop tower display strong oscillations. This phenomenon is due to wave propagation through the sample and the compression device.

Mesoscopic behaviour

The behaviour described in this section is based on observations made in a vertical plane inside the 3D microtomographs. This 2D approach allows us to rapidly supply first results and to orient the latter study in 3D as well as the complete modelling of the porous material. The main assumption beneath this approach is that displacement remains in the planes parallel to the compression axis, i.e., that the foam has negligible horizontal displacement. This can be assumed for two reasons: firstly the Poisson ratio of this foam is close to zero, and secondly displacements of the bead barycentres are vertical in the plane of observation. This hypothesis was confirmed by the material deformation study in several diametral planes.

Figure 9a shows a vertical cross-section of the sample prior to impact. The dimensions of the sample were chosen to correspond exactly to the field of view, but due to the cutting process, the outer surface of the cylinder is irregular and some bead edges are slightly out of the field. The pixels of high intensity correspond to points of dense material (within a bead wall for example). The reconstructed image is of good quality since one can observe the large air bubbles generated during the production of porous beads. The structure of the closed cells is also distinguishable. At a larger scale, the geometry of the compacted beads can be identified as a classical polyhedral structure. The bead sizes are about 2–3 mm and their walls are about 54 μm (11 pixels measured on the image and converted by the scale factor of 1 pixel = 4.91 μm).

In order to analyse the mesoscopic behaviour of the foam, i.e., the deformation of the beads, the bead walls need to be properly identified. The first method consisted in automatically filtering the image to extract the clearest pixels (corresponding to denser areas in the foam). The filter, which consisted in a thresholding of the image gradient, was calibrated to obtain a wall thickness close to the one measured by other techniques (SEM or optical microscopy). However, from this first method, fine walls of air bubbles and cells are falsely identified as bead walls. Further processing is necessary to eliminate these undesirable features (Fig. 9b), rendering this approach fairly time-consuming. A second method, less time consuming, was considered. The structure of the beads in the vertical plane has been represented by a polyhedral structure: segments, having a thickness of 11 pixels (equal to the average thickness of the bead walls) were placed to coarsely fit the bead walls (Fig. 9c). The results of the two methods were compared by measuring the surfaces of the delineated beads. The differences being smaller than 2%, the fastest method, i.e., the second, was used. This process has been then carried out on vertical sections of the sample at each step of the impact (Fig. 10a, b, c and d for sample heights of 9, 7, 5 and 3 mm). For the first impact, the bead structure is accurately approximated by a few segments, but for the other impacts several successive segments are necessary to take into account wall buckling.

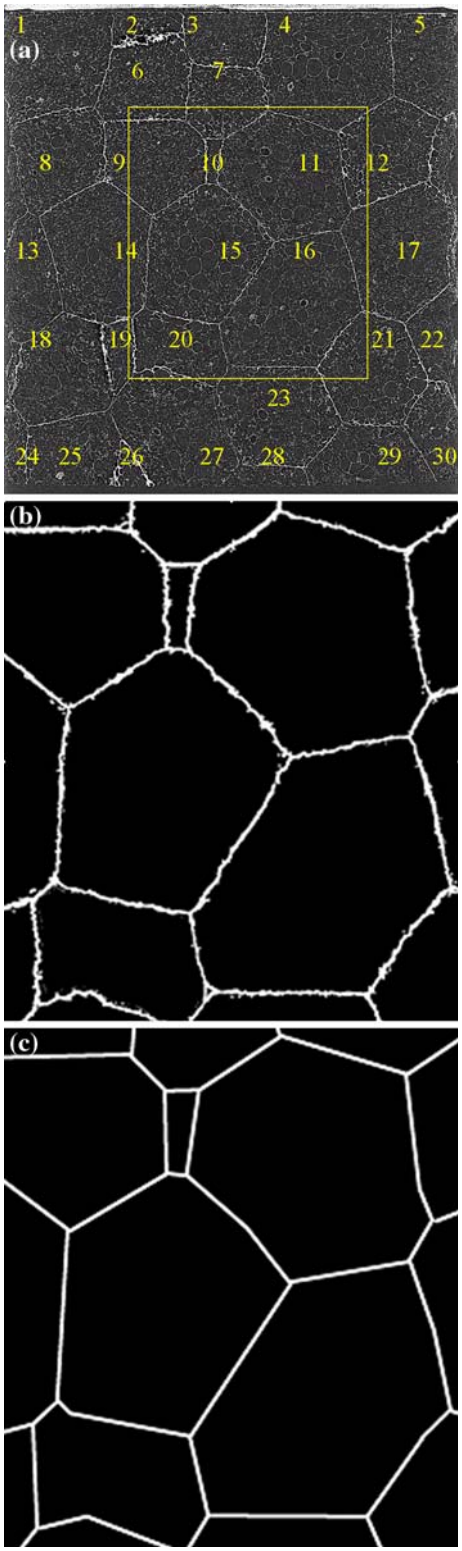

Fig. 9 (**a**) Vertical section of the sample before impact (height = 10 mm, diameter = 10 mm); (**b**) Bead structure extracted after filtering; (**c**) Delineation of the bead structure

At the end of this process, each bead section is represented by a polygon on which various characteristics can be measured (grey levels, surfaces, and polygon barycentre position). From those measurements, pertinent data (density, deformation, bead barycentre displacement) can be estimated for each bead.

Density vs. grey level

Using common image processing software, the average grey level of each polygon was calculated. Theoretically, there is a linear relation between the grey level of a voxel and the density of the corresponding volume element. Indeed, the reconstruction program produces a 3D mapping of μ, the linear attenuation coefficient of the material. The grey level image is obtained by applying the following transformation to this 3D mapping: the grey level attributed to the voxels having a value lower than $\mu_{\min}$ is 0, for the voxels having a value larger than $\mu_{\max}$ it is 255, and in between a linear interpolation is applied. The values of $\mu_{\min}$ and $\mu_{\max}$ are determined by the local range of porosity and the amount of noise in the acquisition. Noting that:

$$\begin{aligned} \mu_{\text{air}} &<< \mu_{\text{pp}} \\ \rho_{\text{air}} &<< \rho_{\text{pp}} \end{aligned} \tag{7}$$

the following relations can be obtained:

$$\begin{aligned} \mu &= (1-\phi)\mu_{\text{pp}} \\ \rho &= (1-\phi)\rho_{\text{pp}} \end{aligned} \tag{8}$$

where ρ is the density, φ the porosity, and subscripts air and pp refer respectively to air and polypropylene.

Combining Eq. (8) and the linear relation between μ and the grey level (between $\mu_{\min}$ and $\mu_{\max}$), grey level and density should be linearly related.

In practice, the variation of the grey level averaged on each bead section is weak and ranges from 77 to 98. The dynamic of measurement, calculated as the ratio of the variation of grey level (98–77) on the measurement range (256) does not exceed 8 %. Using Eq. (8), those values correspond to bead porosities from 98% to 36%, and reveal for the first time a strong heterogeneity at the bead scale (Table 1). However, even if this high variation of porosity is coherent with the visual observations, it is difficult to consider those results as realistic since the noise associated with grey level measurement generates a significant error on local porosity.

Therefore, the grey levels were not used to calculate bead densities, but only to estimate relative variations of density. About 6 classes of grey level were defined (described in Table 1) to highlight the density heterogeneity (Fig.11, where a colour is associated with each class). The result is an image showing a strong heterogeneity in

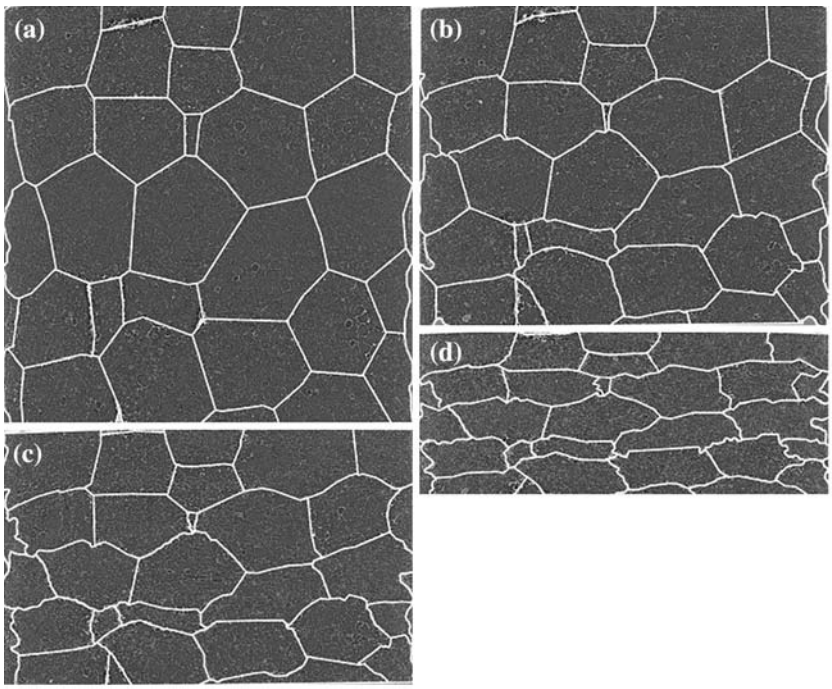

Fig. 10 Foam vertical sections showing the bead structure after the first impact (**a**), after the second (**b**), after the third (**c**), and after the fourth one (**d**)

Table 1 Classification of the pixels by grey level

Classes	Range	Porosity	Density
Class 1	[77; 77.2]	[0.98; 0.978]	[13.4; 18.7]
Class 2	[77.2; 78.2]	[0.978; 0.95]	[18.7; 45.5]
Class 3	[78.2; 79]	[0.95; 0.926]	[45.5; 67]
Class 4	[79; 81.3]	[0.926; 0.857]	[67; 128]
Class 5	[81.3; 83.8]	[0.857; 0.783]	[128; 195]
Class 6	[83.8; 98]	[0.783; 0.36]	[195; 575]

the bead density distribution, the densest beads being located at the vertical border of the sample. This is due to the cutting operation, which was done using a crown saw. The induced radial shear caused a local density increase in the sample periphery.

Bead displacement and deformation

For each impact, the positions of the polygon barycentres were calculated; their displacements are mainly vertical (Fig. 12). Therefore, the barycentre displacement field is not modified by density heterogeneity and the uniaxial compression does not induce transverse deformation. This is not caused by sample confinement because there is no contact with the diametral wall during compression.

Based on this fact, the surface S_{gi} of polygon g after impact i can be compared to its initial value S_{g0} (before the first impact). The surface variation ΔS_{gi0} is calculated in the following way:

$$\Delta S_{gi0} = \frac{S_{gi} - S_{g0}}{S_{g0}} \tag{9}$$

ΔS_{gi0} is a deformation indicator for each bead g (in the vertical plane). Assuming that there is a correlation between ΔS_{gi0} and the bead volume variation (corresponding to the first invariant J_1 equal to the trace of the strain tensor), it is possible to evaluate the volumetric strain

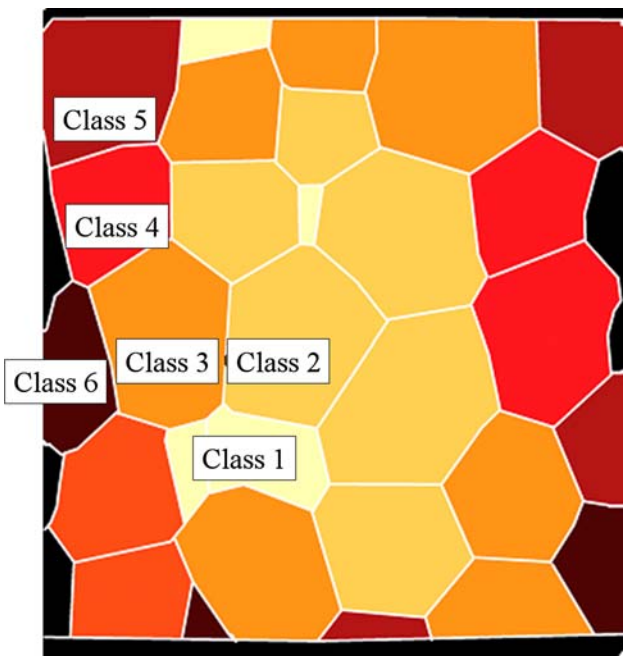

Fig. 11 Density map of the foam structure

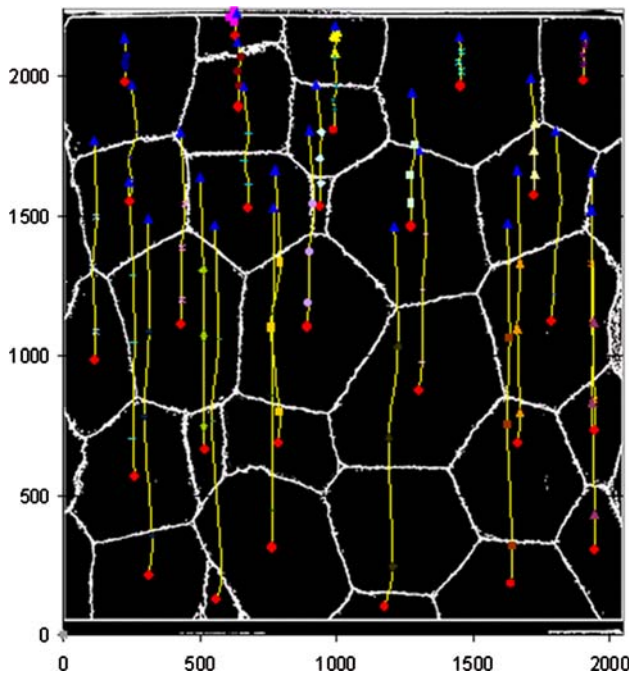

Fig. 12 Displacement of bead barycentres during interrupted impacts

heterogeneity of the bead in the structure. And since the Poisson ratio is close to zero for this foam, this measurement corresponds to the vertical strain ε_g of each bead g.

Comparing the average surface variation $m_i = \langle \Delta S_{gi0} \rangle$ for impact i and the global strain of the sample ($\varepsilon_i = \frac{\Delta h_{i0}}{h_0}$, where h_0 is the sample height and Δh_{i0} its variation during impact i), for the first impact $m_1 = 9\%$ is close to the global deformation $\varepsilon_1 = 10\%$, and for the following impacts, the m_i are strictly equal to the global deformationε_i. This seems to confirm that the study of ΔS_{gi0} can reveal the state of strain for each bead. Afterwards, the vertical strain ε_g of each bead g (due to an impact i) will thus be estimated from ΔS_{gi0}.

First impact

For the first impact ($\varepsilon_1 = 10\%$), the values ε_{g10} are presented in Fig. 13a. Examining the strain ε_{g10} according to the position of the beads, one finds that the damage is layered and mainly localised near the surfaces in contact with the compression device. Beads 1–5 and 27–30 are strongly deformed by this first impact: the maximum variations (–28%, negative since it corresponds to a compression strain) are for beads 2 and 28, the beads around these two beads are among the most deformed. Another layer of beads—18 to 22—seems slightly more deformed than the average whereas the layer comprising beads 6–17 remains almost intact.

Visual inspection of the bead and cell wall deformation corroborates this analysis. Several factors can be suggested to explain this behaviour: the contact with the rigid surfaces of the punches can generate a greater deformation for border beads, but sample preparation can also be evoked. These beads, having been cut, were weakened by the loss of a part of their walls.

Furthermore, no correlation is observed between the bead densities and their deformation. Beads 18 and 20 have

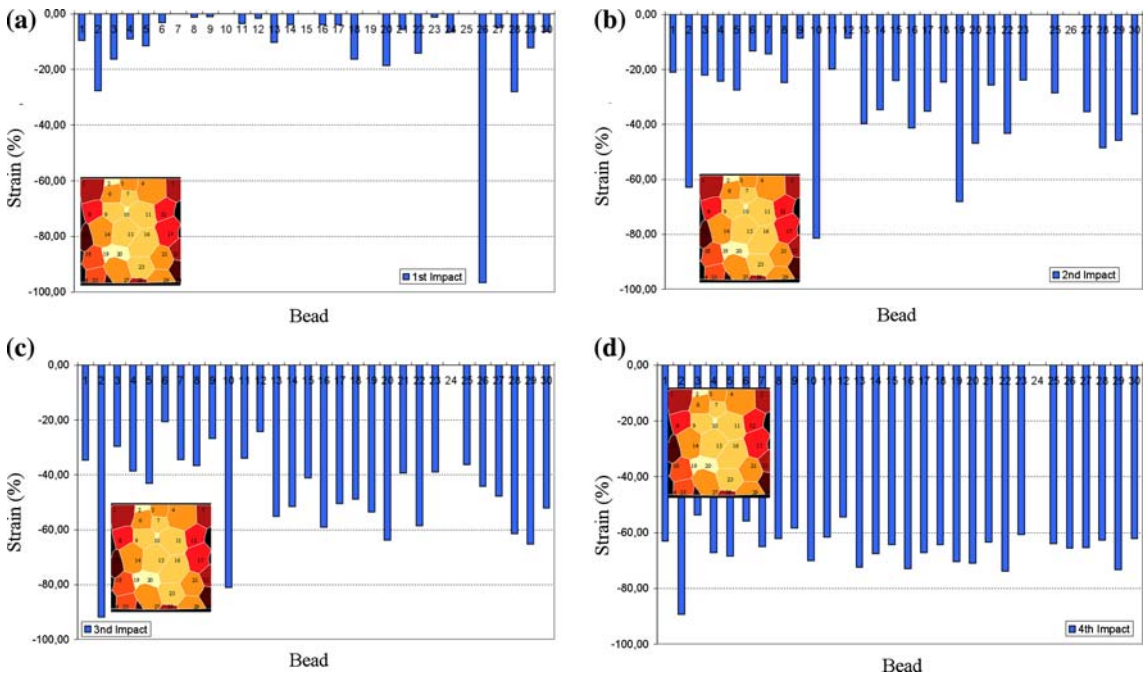

Fig. 13 (**a**) Strain ε_{g10} for each bead g (bead 26 result is discarded since its surface is not representative); (**b**) Strain ε_{g20} for each bead g; (**c**) Strain ε_{g30} for each bead g; (**d**) Strain ε_{g40} for each bead g

equivalent strain levels whereas their densities are very different. In the same way, bead 16 is less deformed than bead 18 whereas its density is lower. Therefore, it seems that density is not a factor affecting bead deformation, the structural effect dominates.

Second impact

After the 2nd impact (Fig. 13b), three strongly deformed zones are observed. Firstly, in the higher part of the sample—beads 1 to 5—the bead strain ε_{g20} is about 20%, lower than the global strain value $\varepsilon_2 = 30\%$. In this layer, bead 2, less dense than the others, is particularly deformed (more than 60% of ε_{g20}), whereas bead 6, of higher density and certainly more rigid, is less deformed and seems to block bead 2 against the punch. As for beads 1 and 3, less deformed than bead 2, there is a strong shear along their boundaries. Deformation mechanisms are more complex than a simple uniaxial compression, as local phenomena induce shear loading within the structure.

Secondly, in the lower zone of the sample, the deformation of beads 25 and 27 through 30 is relatively homogeneous (close to 40%) and slightly higher than ε_2. This shows again that there is not a systematic relation between deformation field and density, as the beads in this area have different densities while their deformations are equivalent.

Lastly, the third strongly compressed area corresponds to the central part of the sample—beads 13–23. The values ε_{g20} for these beads differ significantly as they range from 23% to 48% (except for bead 19 which reaches 70%). Here as well, there is no correlation between bead deformations and densities. Beads 15, 18, 21 and 23 have the lowest strains (around 20%) and have very different densities. Hence this description shows that for dynamic compression, the deformation field of the multi-scale structure does not only depend on the density heterogeneity of the constitutive beads. The least dense beads are not necessarily the most deformed. On the other hand, one can observe that a bead of low density might generate a weakness zone in the material and induce a large deformation of the neighbouring beads. Heterogeneity in the deformation can therefore be explained by structure morphology combined with local weakness. This hypothesis is supported by the strains in the central part of the sample (beads 19 and 20) where beads are more porous. Their deformation is significant, and this mechanical weakness could generate the deformation of the neighbouring beads 18 and 16, which are denser.

Last impacts

The study of the third impact (Fig. 13c) reveals three highly deformed zones which have certainly entered in an irreversible deformation state from the previous impact. Moreover, deformation becomes more homogeneous in these areas: beads 6, 7, 8, 9, 11 and 12 (which were only slightly deformed after the first two impacts) are now more compressed. Their strain ranges from 20% to 36%. These values are however still weaker than the average global value $\varepsilon_3 = 50\%$. Note that, for this significant amount of deformation, some of the beads are still moderately compressed. The densification phase of the cellular material is not yet reached. It is the case after the fourth impact when all the beads are then strongly compressed (Fig. 10d): vertical strains ε_{g40}, shown in Fig. 13d, are homogeneous and higher than 60%.

Conclusion

Dynamic compression tests were carried out on polypropylene foam. The global behaviour of the cellular material has been described for successive interrupted tests. Microtomographic acquisitions (made after each impact) allowed visualising bead wall buckling within the sample.

The strain study of the bead in a vertical plane—and after four impacts—have highlighted the physical phenomena of polymeric foam damage under dynamic compression. There are three stages in the deformation of cellular material: in the first moments of compression, after a very short elastic phase, stronger bead deformation is located near the compression device surface. In the second phase, observed after the second and third impacts, deformations are localised on layers generally perpendicular to the compression direction.

The interrupted impact methodology coupled with microtomographic analysis has been initially conducted in order to reveal a relation between bead density and deformation, where the final objective is to define a simple numerical model of the cellular material structure using finite element code. However, the first results presented here show that the deformation heterogeneity is not simply correlated with the density field; the densest beads are not necessarily the least deformed and vice versa. It seems more accurate to suppose that the most porous beads, generate randomly located weakness zones in the cellular material and then induce local collapse of the structure which are transmitted by layers to the neighbouring beads. It is the combined effect of the structure morphology and of the heterogeneous density field which creates a specific deformation field for a specific dynamic compression. Numerical modelling of the cellular material structure will have to take into account these phenomena to reproduce the foam behaviour.

The next step, a fully 3D analysis of 3D reconstructed images is in progress. However, 3D extraction of the bead

walls of this multi-scale foam is much more difficult than other types of foams that have been more extensively studied, such as metallic foams. For instance, aluminium foam is not multi-scale and the 3D images of the structure have a better contrast and are more readily usable [12].

One of the final objectives of the present study is to obtain a good 3D image of the bead wall structure, requiring the extraction of the bead thick walls from the multi-scale structure. Typical digital image filters are not sufficient to extract these walls: they produce structures with unrealistic porous zones and traces of cells or bubbles having thicker walls (Fig. 5a), which cannot be used to quantify variations of bead volume, strain and even less to obtain a FE mesh of the foam morphology.

To overcome this difficulty, an approach based on a priori information on bead geometry has been evaluated: beads were modelled as polyhedrons whose facets are fitted on the filtered wall structures (Fig. 14). The procedure is not automatised and consequently is very time consuming and laborious. Nevertheless, for the first time it has been possible to follow the 3D deformation for each impact of a single bead within the studied polypropylene foam (Fig. 15). In spite of the quality of the resulting information, applying this procedure to the whole sample can't be envisioned and alternative automatised methods of 3D reconstruction of the bead structure are under development.

The results waited from these reconstruction methods would be used to model more reliably the correlation between the local deformation of the structure and the macroscopic response of the material.

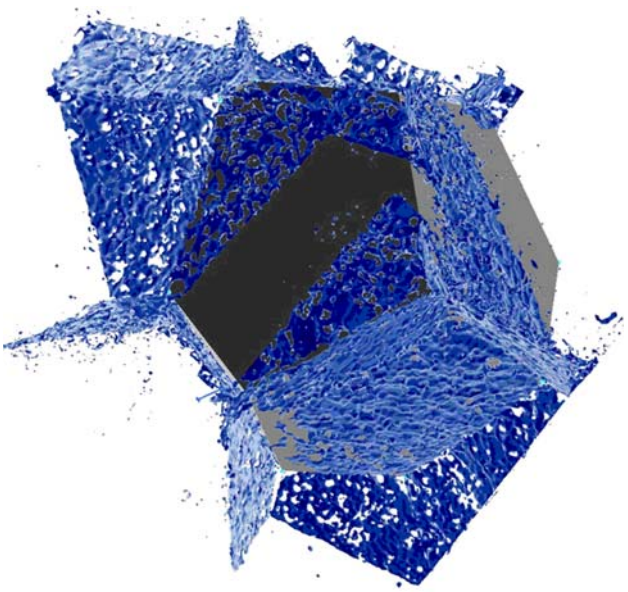

Fig. 14 Bead modelling as polyhedron

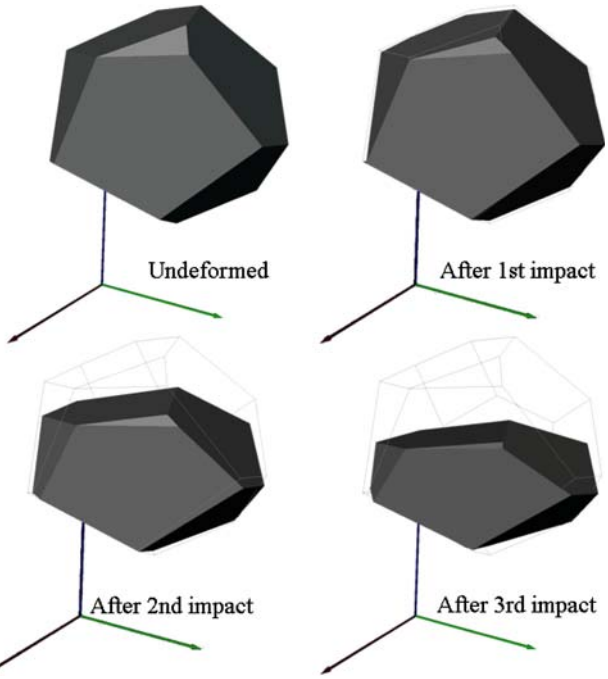

Fig. 15 Strain evolution of a single bead

Acknowledgements We acknowledge the *European Synchrotron Radiation Facility* for provision of synchrotron radiation facilities. Computations and 3D visualisations have been made possible thanks to the computing equipment partly funded by the *Conseil Régional d'Aquitaine*. We would like to thank Gregory Hauss to have modelled with patience and meticulousness a bead of this polymeric foam at different steps of the impact.

References

1. Avalle M, Belingardi G, Montanini R (2001) Int j Impact Eng 25:455
2. Gibson L, Ashby F (1988) Cellular solids. Structures and properties, edn. Cambridge Solid State Science Series
3. Maier M, Huber U, Mkrtchyan L, Fremgen C (2003) Comp Sci Technol 63:2007
4. Zhao H, Elnasri I, Abdennadher S (2005) Int J Mech Sci 47(4–5): 757
5. Viot P, Beani F (2003) Revue des Composites et des Matériaux Avancés 13(3):283, ISBN 2-7462-1117-3
6. Viot P, Beani F, Lataillade J-L (2005) J Mater Sci 40:5829
7. Viot P, Vacher P (2004) Identification of foam behavior under dynamic loading by the use of particle imaging techniques, Revue Matériaux et Techniques, hors série, p 39. ISSN 0032-6895
8. Viot P, Bernard D (2006) J Mater Sci 41:1277
9. Baruchel J, Buffière JY, Maire E, Merle P, Peix G (2000) X-ray tomography in material science. Hermes Sciences Pub, Paris
10. Herman GT (1980) Image reconstruction from projections: the fundamentals of computerized tomography. Academic Press, New York
11. Natterer F (1999) Acta Numer 8:107
12. Marmottant A, Despois JF, Salvo L, Maire E, Bornert M (2005) In-situ X-ray Tomography investigation of replicated Aluminium Foams: quantitative analysis of localisation using 3D strain mapping, Porous metals and metal foaming technology edited by the Japan Institute of Metals ISBN 4-88903-405-6